



Structure and high rate performance of Ni^{2+} doped $\text{Li}_4\text{Ti}_5\text{O}_{12}$ for lithium ion battery



Chunfu Lin ^a, Man On Lai ^a, Li Lu ^{a,*}, Henghui Zhou ^{b, **}, Yuelong Xin ^b

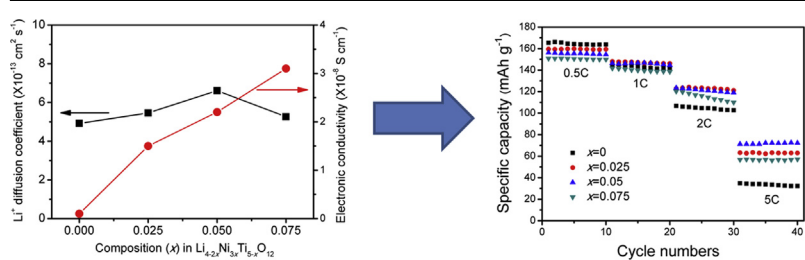
^a Department of Mechanical Engineering, National University of Singapore, 9 Engineering Drive 1, Singapore 117576, Singapore

^b College of Chemistry and Molecular Engineering, Peking University, Beijing 100871, PR China

HIGHLIGHTS

- $\text{Li}_{4-2x}\text{Ni}_{3x}\text{Ti}_{5-x}\text{O}_{12}$ ($0 \leq x \leq 0.25$) from solid-state reaction is systematically studied.
- The effects of material structure on electrochemical properties are investigated.
- The electronic conductivity is largely improved through Ni^{2+} doping.
- $\text{Li}_{3.9}\text{Ni}_{0.15}\text{Ti}_{4.95}\text{O}_{12}$ anode exhibits high rate performance.

GRAPHICAL ABSTRACT



ARTICLE INFO

Article history:

Received 1 November 2012

Received in revised form

10 January 2013

Accepted 11 January 2013

Available online 18 January 2013

Keywords:

Lithium ion battery

Spinel structure

Anode material

Doping

ABSTRACT

$\text{Li}_{4-2x}\text{Ni}_{3x}\text{Ti}_{5-x}\text{O}_{12}$ ($0 \leq x \leq 0.25$) has been synthesized via solid-state reaction. X-ray diffractions (XRD) demonstrate that all doped samples have a spinel structure with $\text{Fd}\bar{3}m$ space group without any impurities. Through further Rietveld refinements, it is shown that both lattice parameter and occupancy of non- Li^+ ions in the 8a sites negligibly change with the amount of Ni^{2+} dopants. Scanning electron microscope reveals that Ni^{2+} doping does not change the morphology of $\text{Li}_4\text{Ti}_5\text{O}_{12}$. The best electronic conductivity of Ni^{2+} doped $\text{Li}_4\text{Ti}_5\text{O}_{12}$ is at least one order of magnitude higher than that of the pristine one, while all samples have similar Li^+ ion diffusion coefficients. The electrochemical performance of Ni^{2+} doped $\text{Li}_4\text{Ti}_5\text{O}_{12}$ shows good rate capability. The specific capacity of $\text{Li}_{3.9}\text{Ni}_{0.15}\text{Ti}_{4.95}\text{O}_{12}$ at 5 C is as high as 72 mAh g^{-1} , while that of the pristine one can only achieve 33 mAh g^{-1} . This improved rate performance can be ascribed to its enhanced electronic conductivity.

© 2013 Elsevier B.V. All rights reserved.

1. Introduction

Stimulated by the urgency of environmental protection and the exhaustion of fossil fuel reserves, more and more attention have been paid to the development of lithium ion batteries with high power density for the applications of large format energy storage system, such as electric vehicles (EVs) or hybrid electrical vehicles (HEVs) [1]. At present, one of the main factors that hinders the

commercialization of EVs/HEVs is the low rate performance of batteries. Therefore, an urgent step for the significant market penetration of EVs/HEVs is the development of a high rate battery system.

Graphite has been proven to be a reliable anode material in commercial lithium ion batteries [2]. However, its rate capability is limited. When the operation current density is large, it suffers from severe polarization causing metallic lithium to deposit on its surface [3,4]. Safety problems will emerge if such process is repeated many times due to the growth of lithium dendrites.

$\text{Li}_4\text{Ti}_5\text{O}_{12}$ has been regarded as an attracting substitute for carbon-based anode in batteries. It has a theoretical capacity of 175 mAh g^{-1} and a high discharge plateau of $1.55\text{--}1.56 \text{ V}$ vs Li/Li^+

* Corresponding author. Tel.: +65 65162236; fax: +65 67791459.

** Corresponding author. Tel./fax: +86 10 62757908.

E-mail addresses: lulu@nus.edu.sg (L. Lu), hhzhou@pku.edu.cn (H. Zhou).

[5,6], avoiding the growth of lithium dendrites. It has a spinel structure with $Fd\bar{3}m$ space group [7]. O^{2-} ions at the 32e sites form a cubic closest packed structure. The tetrahedral 8a sites are occupied by Li^{+} ions, while Li^{+} and Ti^{4+} ions are disordered, filling the octahedral 16d sites in the molar ratio of 1:5. It is noted that the remaining half of the octahedral cation sites in the cubic closest packed structure are vacant (the 16c sites). During discharging, three external Li^{+} ions and the three Li^{+} ions in the 8a sites move to the 16c sites. During charging, the process reverses. During the charging and discharging processes, the robust three-dimensional framework $(LiTi_5)^{16d}(O_{12})^{32e}$ is not changed and its volume change is smaller than 0.1% [8]. Thus, it is considered as a “zero-strain” anode material. Consequently, it has demonstrated excellent cycle life and reversibility.

Nevertheless, a main obstacle that impedes the widespread applications of $Li_4Ti_5O_{12}$ is its poor conduction with associated poor rate performance [9–11]. During the charge and discharge processes, Li^{+} ions intercalate and de-intercalate into the framework of $Li_4Ti_5O_{12}$ lattice accompanied by electrons. Therefore, the conduction depends on Li^{+} ion diffusion coefficient, electronic conductivity and particle size. Larger Li^{+} ion diffusion coefficient, larger electronic conductivity and smaller particle size are favourable for a better conduction. To enhance electronic conductivity, Zr^{4+} [9], Mg^{2+} [10,11], Zn^{2+} [12], Ni^{2+} [13], Al^{3+} [14], Nb^{5+} [15], V^{5+} [16], Ta^{5+} [17], Cr^{3+} [18] and Ni^{3+} [19] doping have been used, and conducting carbon [20], Cu [21] and Ag [22] have also been incorporated to increase electronic conductivity. Zr^{4+} [9], Mg^{2+} [10], Nb^{5+} [15], V^{5+} [16] and Cr^{3+} [18] doping have been shown to improve Li^{+} ion diffusion coefficient. In addition, to reduce Li^{+} ion transportation distance, various types of nanosize $Li_4Ti_5O_{12}$ have been synthesized such as nanoparticles [23–27], nanowires [28], nanorods [29], nanotubes [30], nanosheets [31], porous particles [32,33] and hollow spheres [34]. With suitable doping including Zr^{4+} [9], Nb^{5+} [15] and V^{5+} [16] the particle size can also be reduced.

In this work, we aim to increase intrinsic conductivity by doping methodology. The 3d electrons in Ni^{2+} ion have a $t_{2g}6\ e_g3$ electronic configuration [35]. The electrons in the 3d orbitals can contribute to the improvement in electronic conductivity. Therefore, Ni^{2+} ion is expected to be a promising dopant for $Li_4Ti_5O_{12}$ to improve its rate performance. Thus far, only one paper has focused on the electrochemical characteristics of Ni^{2+} doped $Li_4Ti_5O_{12}$. Kim et al. have investigated the rate performance of $Li_{11/3}Ni_{1/2}Ti_{29/6}O_{12}$ [13]. They have shown that the specific capacity of this heavily Ni^{2+} doped $Li_4Ti_5O_{12}$ is almost double that of pristine material at 5 C. Nevertheless, in this type of Ni^{2+} doped $Li_4Ti_5O_{12}$, every two Li^{+} ions and every one Ti^{4+} ion are substituted by three Ni^{2+} ions. Obviously, when the amount of dopant increases, the molecular weight increases, and the theoretical capacity decreases. Moreover, the study on this doping is not complete. It is still unclear how electrochemical properties can be related to the material structure. Therefore, it is highly desirable to systematically research on the electrochemical performance of $Li_4Ti_5O_{12}$ with light Ni^{2+} doping. $Li_{4-2x}Ni_{3x}Ti_{5-x}O_{12}$ ($0 \leq x \leq 0.25$) synthesized via a facile solid-state reaction method is systematically studied in the current research. The effects of doping on electrochemical properties are also investigated.

2. Experimental

2.1. Preparation of materials

All samples were prepared using a solid-state reaction method. In a typical fabrication processing, Li_2CO_3 (Merck, 99.99%), TiO_2 (Sigma–Aldrich, 99.9%) and NiO (Aldrich, 76–77%Ni) powders were

employed as Li^{+} , Ti^{4+} and Ni^{2+} sources respectively. Appropriate amounts of these sources were firstly ball-milled for 0.5 h in a Spex ball-milling machine to homogenously mix the powders. In all cases, 3 mol% excessive Li_2CO_3 was added to compensate for Li_2O evaporation during the synthesis at high temperature. Then, the milled mixtures were calcined at 800 °C for 4 h in a muffle furnace in air.

2.2. Characterization

The structures of the as-sintered powders were determined using an X-ray diffractometer on a Shimazu XRD-6000/7000 with a $Cu\ K\alpha$ radiation. The continuous-scan data were collected between 15° and 70° (2θ) at a scan speed of 2°/min. The high quality data for Rietveld refinements were recorded from Shimazu XRD-7000 in an angle interval 15°–125° using step scan with 8 s per step. Rietveld refinements were carried out using the GSAS program with the EXPGUI interface [36,37]. The refined instrumental and structural parameters were: scale factor, background parameters, zero-shift, unit cell parameters, atomic fractional coordinates, atomic occupancies, atomic isotropic displacement parameters and profile parameters. The site occupancies were constrained to the designed chemical formulas. The site occupancy of oxygen atoms was fixed to be 1.

Surface solid-state chemistry of particles was characterized by X-ray photoelectron spectroscopy (XPS, Kratos Ultra DLD, Shimadzu, Japan) in fixed transmission mode with a pass energy of 80 mV and the binding energy ranged from 0 to 1100 eV. The morphologies and microstructures of the samples were examined by a field emission scanning electron microscopy (FESEM, JEOL JSM-6700F) operating at 5 kV.

2.3. Electrochemical tests

Electrochemical performances of the as-synthesized materials were tested using a two-electrode coin-type half-cell at room temperature. Electrodes were prepared by mixing 80 wt% active material with 10 wt% super P conductive carbon (TIMCAL Ltd.), and 10 wt% polyvinylidene fluoride (PVDF, Aldrich) in N-methylpyrrolidone (NMP, Sigma–Aldrich) solvent at a rotational speed of 1500 rpm for 12 h to form a homogeneous slurry. The slurry was coated on the Al foil. The coated electrodes were dried at 120 °C in a vacuum chamber for overnight and then pressed by a rolling machine. Thereafter, 2016 coin cells (MTI corporation) were assembled in a glove box filled with ultra-pure argon gas using the as-prepared working electrodes, Li metal as the counter and reference electrode, Celgard 2400 as the separator, and 1 M $LiPF_6$ in ethylene carbonate (EC)-dimethyl carbonate (DMC)-diethylene carbonate (DEC) (1:1:1 in weight, DAN VEC) as the electrolyte. The discharge-charge tests of the cells were carried out between 1.0 and 2.5 V using a Neware Battery Test System. The cells were firstly discharged/charged at 0.1 C where current density of 1 C is equal to 175 $mA\ g^{-1}$ for 1 cycle, and then cycled at 0.5 C, 1 C, 2 C and 5 C for 10 cycles with a 5 min step-interval between each cycle.

To measure Li^{+} ion diffusion coefficient, electrochemical impedance spectroscopy (EIS) measurements were performed with 5 mV ac signal and a frequency range from 10^5 to 0.1 Hz using a Solartron Analytical 1470E CellTest System coupled with a Solartron Analytical 1400 CellTest System. All measurements were carried out after the cells being discharged to 50% state of discharge followed by two cycles.

The specimens used for conductivity measurements were prepared by pressing the same precursor powders in Section 2.1 into pellets of 10.25 mm diameter at 50 MPa. Cold compacts were then calcined at 650 °C for 5 h followed by sintering at

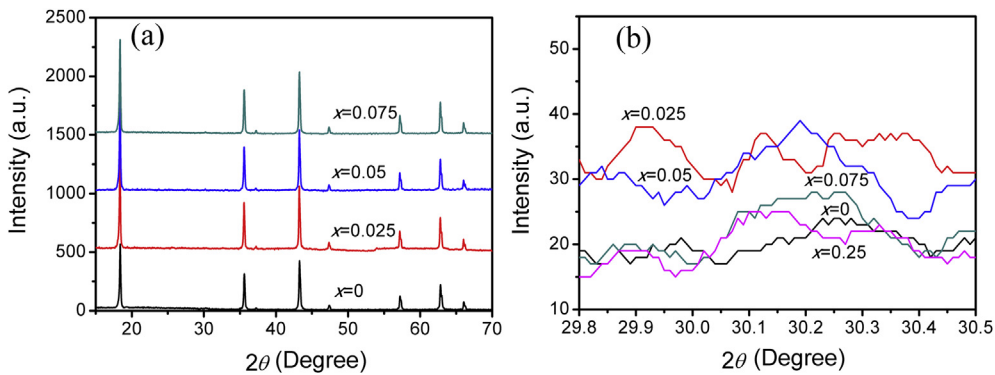


Fig. 1. (a) X-ray diffraction patterns of $\text{Li}_{4-2x}\text{Ni}_{3x}\text{Ti}_{5-x}\text{O}_{12}$ ($0 \leq x \leq 0.075$); (b) comparison of (220) peaks of $\text{Li}_{4-2x}\text{Ni}_{3x}\text{Ti}_{5-x}\text{O}_{12}$ ($0 \leq x \leq 0.25$).

900 °C for 48 h for densification. The thickness of these pellets was about 0.94 mm. All the sintered pellets had similar density of approximately 85–90%. Gold was sputtered to both sides of the pellets after grinding of the surfaces using sand papers. Electronic conductivity was measured using an Analytical 1470E CellTest System under a constant voltage of 50 mV for 3 h until the currents became stabilized.

3. Results and discussion

3.1. Crystal structure analysis

XRD spectra of $\text{Li}_{4-2x}\text{Ni}_{3x}\text{Ti}_{5-x}\text{O}_{12}$ ($0 \leq x \leq 0.25$) samples with enlarged (220) peaks are shown in Fig. 1(a) and (b). All peaks in Fig. 1(a) can be indexed as cubic spinel structure with $\text{Fd}\bar{3}m$ space group (JCPDS 26-1198). The sharp peaks indicate good crystallinity of all the samples and no impurity-phase were detected, demonstrating that Ni^{2+} ions have been successfully introduced into the

lattice structure of $\text{Li}_4\text{Ti}_5\text{O}_{12}$. In this spinel structure, the intensity of the (220) peak at approximately 30.2° is determined by the scattering power of the cations in the 8a sites. For all the samples, the (220) peak cannot be observed, indicating that the 8a sites are almost full of Li^+ ions with very small scattering factor and that very few non- Li^+ ions occupy the 8a sites.

To better understand the structure in detail, Rietveld refinements were employed. Fig. 2 presents the final observed, calculated, and error profiles for $\text{Li}_{4-2x}\text{Ni}_{3x}\text{Ti}_{5-x}\text{O}_{12}$ ($x = 0, 0.025, 0.05$ and 0.075) while the results of the crystal structure analysis are listed in Table 1. Several constraints for the refinements have been assumed. First, the site occupancies fulfilled the stoichiometric compositions of $\text{Li}_{4-2x}\text{Ni}_{3x}\text{Ti}_{5-x}\text{O}_{12}$ in which all Ni-ions have +2 oxidation state. The XPS results of $\text{Li}_{4.85}\text{Ni}_{0.225}\text{Ti}_{4.925}\text{O}_{12}$ given in Fig. 3 show that the $2p_{3/2}$ peak of Ni^{3+} is much smaller than that of Ni^{2+} , which is well consistent with existing results [13]. Therefore, it is reasonable to assume that Ni^{3+} ions in $\text{Li}_{4-2x}\text{Ni}_{3x}\text{Ti}_{5-x}\text{O}_{12}$ ($0 \leq x \leq 0.25$) can be negligible. Second, all ions

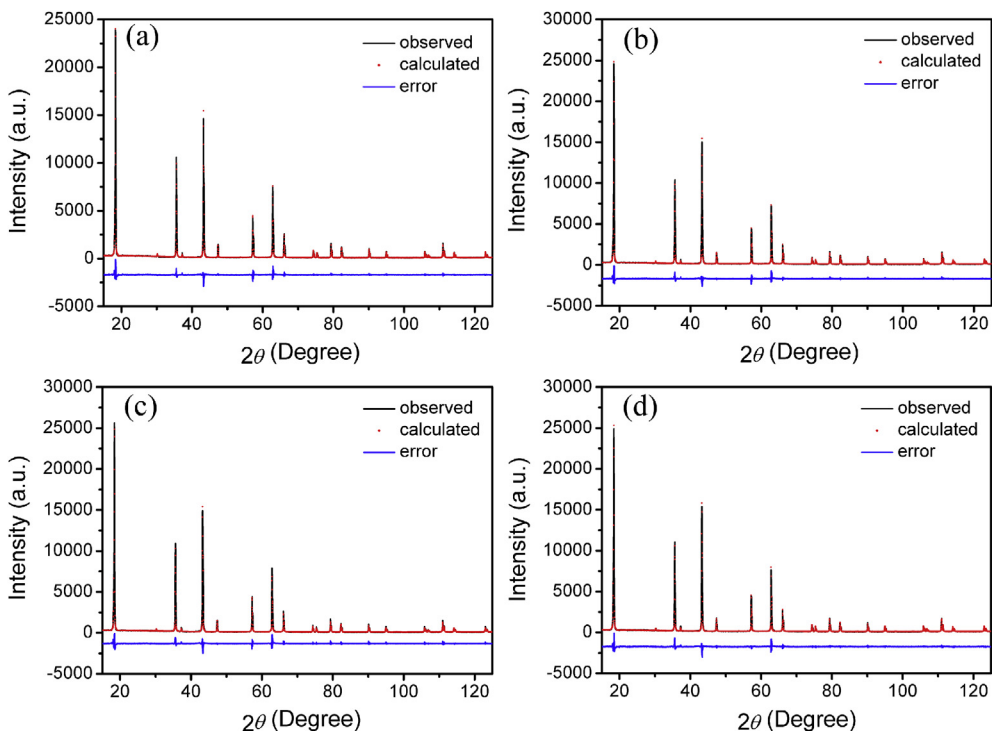


Fig. 2. Final observed, calculated, and error profiles with Rietveld refinements for $\text{Li}_{4-2x}\text{Ni}_{3x}\text{Ti}_{5-x}\text{O}_{12}$ with (a) $x = 0$, (b) $x = 0.025$, (c) $x = 0.05$ and (d) $x = 0.075$.

Table 1Results of crystal structure analysis by Rietveld refinements in $\text{Li}_{4-2x}\text{Ni}_{3x}\text{Ti}_{5-x}\text{O}_{12}$ ($x = 0, 0.025, 0.05$ and 0.075).

Spinel $\text{Li}_{4-2x}\text{Ni}_{3x}\text{Ti}_{5-x}\text{O}_{12}$, space group: $\text{Fd}\bar{3}m$ (cubic)					
Composition	x	0	0.025	0.05	0.075
Structure order		$(\text{Li}_{2.997}\text{Ti}_{0.003})^{8a}$ $(\text{Li}_{1.003}\text{Ti}_{4.997})^{16d}\text{O}_{12}^{32e}$	$(\text{Li}_3)^{8a}(\text{Li}_{0.95}\text{Ni}_{0.075}\text{Ti}_{4.975})^{16d}\text{O}_{12}^{32e}$	$(\text{Li}_{2.997}\text{Ti}_{0.003})^{8a}$ $(\text{Li}_{0.903}\text{Ni}_{0.15}\text{Ti}_{4.947})^{16d}\text{O}_{12}^{32e}$	$(\text{Li}_{2.997}\text{Ti}_{0.003})^{8a}$ $(\text{Li}_{0.853}\text{Ni}_{0.225}\text{Ti}_{4.922})^{16d}\text{O}_{12}^{32e}$
Lattice parameter	$a/\text{\AA}$	8.36107(5)	8.36121(5)	8.36093(6)	8.36111(5)
8a	Li1	f	0.999(3)	1.000(2)	0.999(2)
	Ti1		0.001(3)	0.000(2)	0.001(2)
16d	Li2		0.167(2)	0.158(1)	0.151(1)
	Ti2		0.833(2)	0.829(1)	0.824(1)
	Ni		—	0.0125(—)	0.025(—)
32e	O		1(—)	1(—)	1(—)
R_{wp}		0.1032	0.1011	0.1054	0.0943
R_p		0.0782	0.783	0.0815	0.0730
χ^2		3.012	2.999	3.378	2.826

f: site occupancy, R_{wp} : weighted profile residual, R_p : profile residual, and χ^2 : goodness of fit.

had the same isotropic temperature factors. Finally, the distribution of ions in the spinel structure was fixed as follows: O^{2-} ions were fixed at the 32e sites; Li^+ and Ti^{4+} ions were located at both the 8a and the 16d sites while Ni^{2+} ions only occupied the 16d sites. In principle, Ni^{2+} ions may be distributed at both the 8a and the 16d sites. However, the refinements in this case could not proceed due to the similarity in scattering factors of Ni^{2+} and Ti^{4+} ions. Ni^{2+} ion has larger octahedral site preference energy (OSPE, 86.25 kJ mol^{-1}) than Ti^{4+} ion (0 kJ mol^{-1}) [35], indicating that Ni^{2+} ion has higher tendency to stay at the 16d sites than Ti^{4+} ion. Therefore, it is reasonable to assume that Ni^{2+} ions only occupied the 16d sites, while Ti^{4+} ions occupied both the 8a and the 16d sites.

In all the four samples, the occupancy of Ti^{4+} ions in the 8a sites is negligible, confirming that Ni^{2+} doping hardly introduces non- Li^+ ions into the 8a sites. Pristine $\text{Li}_4\text{Ti}_5\text{O}_{12}$ has a lattice parameter of 8.3611 \AA consistent with that previously reported [16–18]. The variation of lattice parameter is within 0.01%, indicating that Ni^{2+} doping cannot significantly impact the lattice parameter. This phenomenon may be ascribed to the ion-size effect. For $\text{Li}_{4-2x}\text{Ni}_{3x}\text{Ti}_{5-x}\text{O}_{12}$, almost all the substitutions occur in the 16d sites. In the 16d sites, every two Li^+ ions (0.76 \AA) and every one Ti^{4+} ion (0.605 \AA) are replaced by three Ni^{2+} ions (0.69 \AA) [38], $2 \times 0.76 + 1 \times 0.605 \approx 3 \times 0.69$, resulting in negligible difference in lattice parameter.

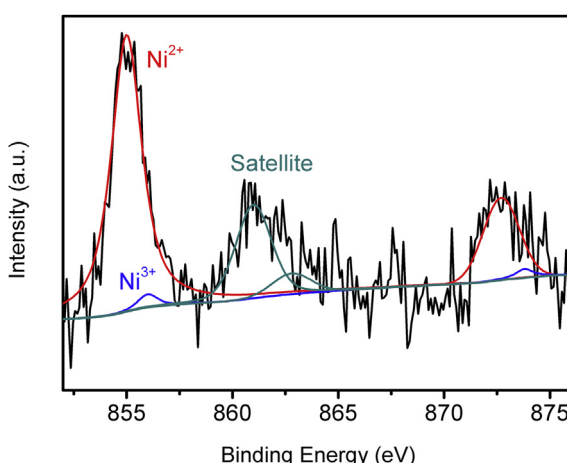
3.2. Particle morphology

The powder morphology of $\text{Li}_{4-2x}\text{Ni}_{3x}\text{Ti}_{5-x}\text{O}_{12}$ ($x = 0, 0.025, 0.05$ and 0.075) calcined at 800 $^\circ\text{C}$ for 4 h in air is displayed in Fig. 4. All the samples have similar morphologies. There is almost no change in morphologies after Ni^{2+} doping. The particle size, with a wide distribution from less than 100 nm to more than 1000 nm, has a medium value of approximately 500 nm.

3.3. Li^+ ion diffusion coefficient measurement

The conductivity of electrode material is a very important factor in evaluating the rate performance of cell. Electrochemical impedance spectroscopy (EIS) was employed to study the influence at different levels of doping in $\text{Li}_{4-2x}\text{Ni}_{3x}\text{Ti}_{5-x}\text{O}_{12}$ ($x = 0, 0.025, 0.05$ and 0.075) samples. Fig. 5(a) shows the Nyquist plots of the impedance response of $\text{Li}_{4-2x}\text{Ni}_{3x}\text{Ti}_{5-x}\text{O}_{12}$ ($x = 0, 0.025, 0.05$ and 0.075) electrodes. To better understand the plots, the AC impedance spectra were fitted using an equivalent circuit shown in Fig. 5(b) [9,10]. The circuit is comprised of a series resistance (R_s), a charge-transfer resistance (R_{ct}), a constant phase element (CPE), and a Warburg impedance (W). R_s indicates the ohmic resistance of the cell. R_{ct} is the electron transfer resistance at the active interface. CPE reflects the interfacial capacitance. W is described as Warburg impedance caused by a semi-infinite diffusion of Li^+ ion in the electrolyte. The fitted results are tabulated in Table 2. It can be seen that the R_s values of all the samples investigated are similar, whereas the R_{ct} values vary largely with different samples. Ni^{2+} doped samples exhibit lower R_{ct} values than that of pristine $\text{Li}_4\text{Ti}_5\text{O}_{12}$, indicating that the doped samples have higher conductivity than pristine counterpart. Among all the samples, $\text{Li}_{3.9}\text{Ni}_{0.15}\text{Ti}_{4.95}\text{O}_{12}$ has the lowest charge-transfer resistance.

The plot of real impedance versus reciprocal square root of the lower angular frequency $\omega^{-0.5}$ is illustrated in Fig. 5(c), from which the value of Warburg impedance coefficient σ_w can be obtained according to Equation 1. Li^+ ion diffusion coefficient D can be calculated from Equation 2 [9,10]. The dependency tendency of Li^+ ion diffusion coefficient D on composition x is given in Fig. 6. Pristine $\text{Li}_4\text{Ti}_5\text{O}_{12}$ electrode has a Li^+ ion diffusion coefficient of $4.92 \times 10^{-13} \text{ cm}^2 \text{ s}^{-1}$, consistent with previous reports [9,10]. All the doped samples exhibit Li^+ ion diffusion coefficients similar to pristine one, although the $\text{Li}_{3.9}\text{Ni}_{0.15}\text{Ti}_{4.95}\text{O}_{12}$ sample has the largest value. These similar D values may be ascribed to their crystalline characteristics. It is known that Li^+ ions transport in 3-dimensional 8a–16c–8a pathways in this spinel structure with $\text{Fd}\bar{3}m$ space group during the discharging and charging processes [39]. Li^+ ions have to

Fig. 3. XPS spectra of Ni 2p core levels of $\text{Li}_{4.85}\text{Ni}_{0.225}\text{Ti}_{4.925}\text{O}_{12}$.

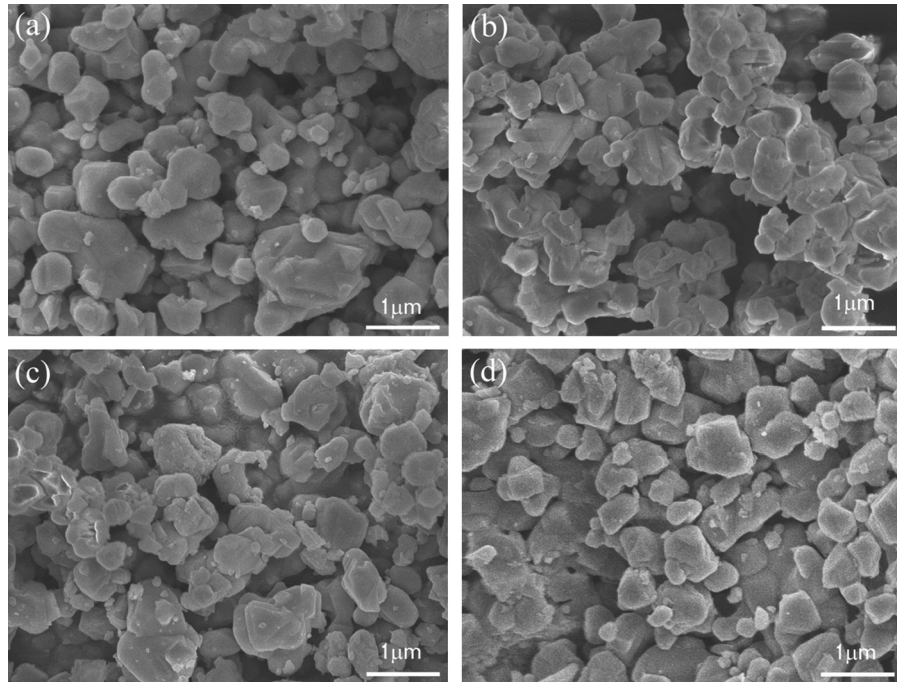


Fig. 4. FESEM images of as-synthesized $\text{Li}_{4-2x}\text{Ni}_{3x}\text{Ti}_{5-x}\text{O}_{12}$ with (a) $x = 0$, (b) $x = 0.025$, (c) $x = 0.05$ and (d) $x = 0.075$.

migrate through the oxygen planes located between the 8a sites and the 16c sites, which is the Li^+ ion transportation bottle neck. In this oxygen closest packed structure, small variation in lattice parameter implies that the distance between the nearest neighbouring O^{2-} ions

is hardly changed, which can lead to the similar values of Li^+ ion diffusion coefficient of the active materials in the cell.

$$Z' = R_s + R_{ct} + \sigma_W \omega^{-0.5} \quad (1)$$

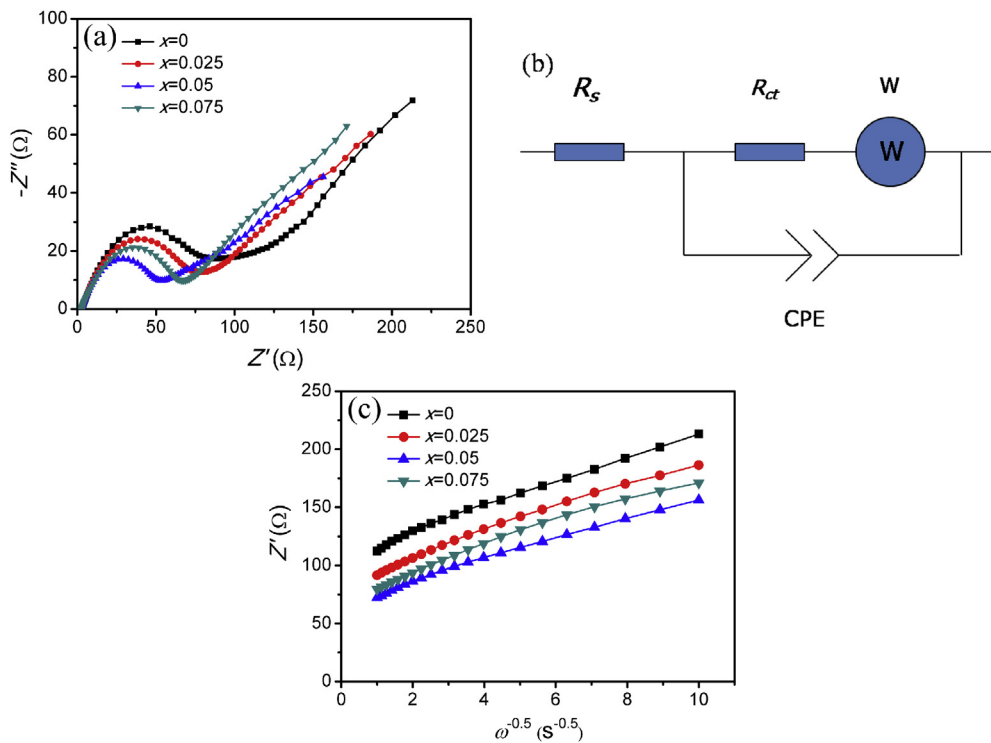


Fig. 5. (a) Nyquist plots for impedance response of $\text{Li}_{4-2x}\text{Ni}_{3x}\text{Ti}_{5-x}\text{O}_{12}$ ($x = 0, 0.025, 0.05$ and 0.075) electrodes. (b) Equivalent circuit used to fit the EIS. R_s : ohmic resistance of the battery; R_{ct} : charge-transfer resistance; CPE: interfacial capacitance; W : Warburg impedance. (c) Relationship between real impedance with low frequency for $\text{Li}_{4-2x}\text{Ni}_{3x}\text{Ti}_{5-x}\text{O}_{12}$ ($x = 0, 0.025, 0.05$ and 0.075) electrodes.

Table 2

Impedance parameters of the $\text{Li}_{4-2x}\text{Ni}_{3x}\text{Ti}_{5-x}\text{O}_{12}$ ($x = 0, 0.025, 0.05$ and 0.075) electrodes.

Samples	R_s (Ω)	R_{ct} (Ω)	σ_w ($\Omega \text{ s}^{-0.5}$)	D ($\text{cm}^2 \text{ s}^{-1}$)
$\text{Li}_4\text{Ti}_5\text{O}_{12}$	3.23	89.3	10.9	4.92×10^{-13}
$\text{Li}_{3.95}\text{Ni}_{0.075}\text{Ti}_{4.975}\text{O}_{12}$	2.81	64.3	10.7	5.46×10^{-13}
$\text{Li}_{3.9}\text{Ni}_{0.15}\text{Ti}_{4.95}\text{O}_{12}$	2.55	55.7	9.25	6.61×10^{-13}
$\text{Li}_{3.85}\text{Ni}_{0.225}\text{Ti}_{4.925}\text{O}_{12}$	2.81	70.1	10.6	5.26×10^{-13}

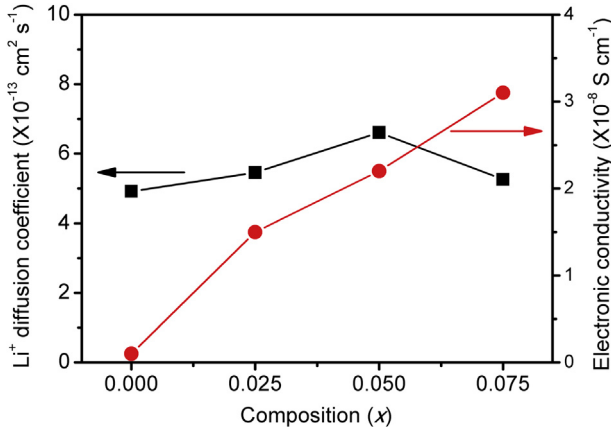


Fig. 6. Variation in Li^+ ion diffusion coefficient and electronic conductivity as a function of composition x in $\text{Li}_{4-2x}\text{Ni}_{3x}\text{Ti}_{5-x}\text{O}_{12}$ ($0 \leq x \leq 0.075$).

$$D = \frac{R^2 T^2}{2A^2 F^4 \sigma_w^2 C^2} \quad (2)$$

where Z is the real part of the impedance, σ_w , the Warburg impedance coefficient, ω , the angular frequency, R , the gas constant, T , the absolute temperature, A , the surface area, F , the Faraday's constant, and C_{Li^+} , the molar concentration of Li^+ ions.

3.4. Electronic conductivity

Fig. 6 also illustrates the dramatic increase in electronic conductivity that can be imparted to $\text{Li}_{4-2x}\text{Ni}_{3x}\text{Ti}_{5-x}\text{O}_{12}$ by Ni^{2+} doping. The dense pellets were achieved by sintering the precursor powders at 900°C . The as-prepared samples from 900°C and 800°C have similar structural characteristics (See Supporting Information). Thus the electronic conductivity obtained from the pellets sintered at 900°C is a good approximation to that at 800°C . The electronic conductivity of pristine $\text{Li}_4\text{Ti}_5\text{O}_{12}$ is very low ($<1 \times 10^{-9} \text{ S cm}^{-1}$) so that it could not be accurately determined within the resolution of the Solartron Analytical 1470E CellTest System. The electronic conductivity monotonically increases with x , reaching a large value of $3.1 \times 10^{-8} \text{ S cm}^{-1}$ ($x = 0.075$), in a good agreement with Kim et al.'s results [13]. This value is larger than those of Al^{3+} doped, Ga^{3+} doped, Co^{3+} doped, Mg^{2+} and Al^{3+} codoped, and Ta^{5+} doped $\text{Li}_4\text{Ti}_5\text{O}_{12}$ with similar doping levels shown in Table 3 [17,40]. It is obvious that 3d transition metal ion Ni^{2+} doping can greatly improve the electronic conductivity.

Table 3

Comparison of electronic conductivity using various dopings. Electronic conductivity was measured using the same method [17,40].

Nominal formula	$\text{Li}_4\text{Ti}_5\text{O}_{12}$	$\text{Li}_{3.95}\text{Ni}_{0.075}\text{Ti}_{4.975}\text{O}_{12}$	$\text{Li}_{3.9}\text{Ni}_{0.15}\text{Ti}_{4.95}\text{O}_{12}$	$\text{Li}_{3.85}\text{Ni}_{0.225}\text{Ti}_{4.925}\text{O}_{12}$	$\text{Li}_{3.95}\text{Al}_{0.15}\text{Ti}_{4.9}\text{O}_{12}$	$\text{Li}_{3.95}\text{Ga}_{0.15}\text{Ti}_{4.9}\text{O}_{12}$	$\text{Li}_{3.95}\text{Co}_{0.15}\text{Ti}_{4.9}\text{O}_{12}$	$\text{Li}_{3.9}\text{Mg}_{0.1}\text{Al}_{0.15}\text{Ti}_{4.85}\text{O}_{12}$	$\text{Li}_4\text{Ta}_{0.05}\text{Ti}_{4.95}\text{O}_{12}$
Electronic conductivity (S cm^{-1})	$<1 \times 10^{-9}$	1.5×10^{-8}	2.2×10^{-8}	3.1×10^{-8}	1.1×10^{-8}	2.0×10^{-9}	1.3×10^{-9}	7.9×10^{-9}	1×10^{-9}

Previous reports showed that electronic conduction in spinel oxides containing transition metal ions is dominated by localized d electrons hopping among the octahedral (16d) cations [41–44]. Pristine $\text{Li}_4\text{Ti}_5\text{O}_{12}$ is an insulator since there are no electrons in the Ti^{4+} ($t_{2g}0 \text{ e}_g0$) 3d orbitals. In contrast, Ni^{2+} ($t_{2g}6 \text{ e}_g3$) ions in the 16d sites supply the charge carriers (electrons) in the doped $\text{Li}_4\text{Ti}_5\text{O}_{12}$. Therefore, the electronic conductivity of $\text{Li}_4\text{Ti}_5\text{O}_{12}$ is greatly enhanced upon Ni^{2+} doping. More Ni^{2+} ions can supply more electrons, leading to larger electronic conductivity.

3.5. Charge/discharge performance at 0.5 C

Fig. 7 plots the second specific charge and discharge capacities of the cells prepared using $\text{Li}_{4-2x}\text{Ni}_{3x}\text{Ti}_{5-x}\text{O}_{12}$ ($x = 0, 0.025, 0.05$ and 0.075) in the potential range of $1-2.5 \text{ V vs Li/Li}^+$ at 0.5 C . During the discharge, the potential drops quickly down to a flat discharge plateau of approximately $1.56 \text{ V vs Li/Li}^+$ and a flat charge plateau at about 1.6 V vs Li/Li^+ can also be observed. This suggests a two-phase reaction based on $\text{Ti}^{3+}/\text{Ti}^{4+}$ redox couple [31]. No other charge/discharge plateaus were observed. The $1.56/1.6 \text{ V vs Li/Li}^+$ plateau contributes more than 90% of the total discharge/charge capacity. The specific capacity decreases when the doping amount increases. At such low rate, electrons and Li^+ ions have adequate time to conduct and diffuse respectively. Thus, the maximum accessible capacity of the active material can be achieved, which may be determined by the theoretical capacity of the active material. The theoretical capacity of $\text{Li}_{4-2x}\text{Ni}_{3x}\text{Ti}_{5-x}\text{O}_{12}$ is calculated as $80400/(460 + 114x) \text{ mAh g}^{-1}$. Obviously, when x increases, the theoretical capacity decreases. Therefore, pristine $\text{Li}_4\text{Ti}_5\text{O}_{12}$ has the largest capacity of 164 mAh g^{-1} , while $\text{Li}_{3.85}\text{Ni}_{0.225}\text{Ti}_{4.925}\text{O}_{12}$ has 150 mAh g^{-1} .

3.6. Rate performance

High rate performance is one of the most important electrochemical characteristics of batteries for EVs/HEVs. The second discharge-charge profiles of $\text{Li}_{4-2x}\text{Ni}_{3x}\text{Ti}_{5-x}\text{O}_{12}$ ($x = 0, 0.025, 0.05$ and 0.075) samples at different rates from 0.5 C to 5 C are presented in Fig. 8. It can be clearly observed that all discharge plateaus monotonically drop due to increasing polarization when the rate increases. For pristine $\text{Li}_4\text{Ti}_5\text{O}_{12}$, with increasing rate, the discharge plateau slowly becomes inconspicuous so that no obvious discharge plateau can be found at 5 C . For each Ni^{2+} doped $\text{Li}_4\text{Ti}_5\text{O}_{12}$, however, an obvious discharge plateau is always observed even at a high rate of 5 C . Meanwhile, all discharge and charge capacities decrease with rates.

Fig. 9 reveals the rate and cyclic performance of the four samples at different rates. It can be seen that the variation in capacity for all the samples is not apparent at low rates (under 1 C). As discussed in Section 3.5, when the rate is low, Li^+ ions and electrons have adequate time to diffuse and conduct respectively, which minimize the difference among the capacities at low rates. It can be observed that pristine $\text{Li}_4\text{Ti}_5\text{O}_{12}$ displays the largest capacity among all the four samples at 0.5 C . When the rate increases, however, its capacity quickly decreases. At 1 C , it is 143 mAh g^{-1} , 105 mAh g^{-1} at 2 C ; and at 5 C , its remained capacity is only 33 mAh g^{-1} . In contrast, as revealed in Fig. 9, in spite of their relatively lower capacities at 0.5 C ,

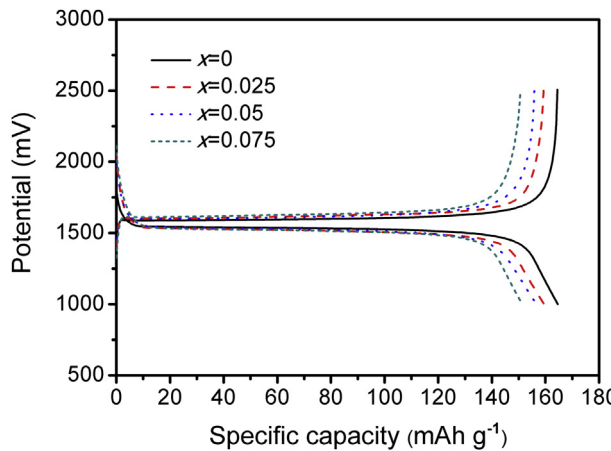


Fig. 7. Second discharge–charge curves of $\text{Li}_{4-2x}\text{Ni}_{3x}\text{Ti}_{5-x}\text{O}_{12}$ ($x = 0, 0.025, 0.05$ and 0.075) samples at 0.5 C (identical discharge/charge rates were used).

the doped samples reveal much less capacity degradation than that of pristine one with the rate increases. For example, at 2 C , the capacities of $\text{Li}_{3.95}\text{Ni}_{0.075}\text{Ti}_{4.975}\text{O}_{12}$, $\text{Li}_{3.9}\text{Ni}_{0.15}\text{Ti}_{4.95}\text{O}_{12}$ and $\text{Li}_{3.85}\text{Ni}_{0.225}\text{Ti}_{4.925}\text{O}_{12}$ are 123 , 121 and 115 mAh g^{-1} respectively; and at 5 C , they are 63 , 72 and 56 mAh g^{-1} . For clearer observation, the relative capacities of all the samples as a function of rate are provided in Fig. 10, in which the capacities determined at 0.5 C are taken as standard.

These results indicate that Ni^{2+} doping impairs the capacity of $\text{Li}_4\text{Ti}_5\text{O}_{12}$ at low rates, but can obviously enhance its rate performance. In this research, since all the samples have similar morphologies and Li^+ ion diffusion coefficients, the rate performance of the active materials is determined by their electronic

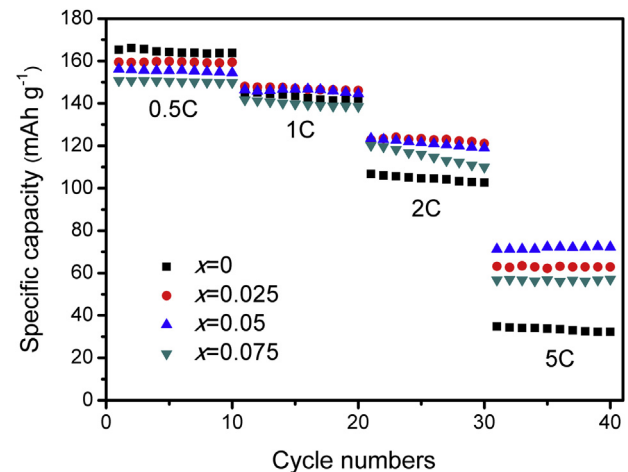


Fig. 9. Rate and cyclic performance of $\text{Li}_{4-2x}\text{Ni}_{3x}\text{Ti}_{5-x}\text{O}_{12}$ ($x = 0, 0.025, 0.05$ and 0.075) samples at different rates: the first 10 cycles at 0.5 C , second at 1 C , third at 2 C and fourth at 5 C (identical discharge/charge rates were used).

conductivity. The electronic conductivity in the doped materials can facilitate the charge-transfer reaction in the cathodes, resulting in good rate performance. It is worth noting that, as shown in Fig. 10, $\text{Li}_{3.9}\text{Ni}_{0.15}\text{Ti}_{4.95}\text{O}_{12}$ has the best rate performance, indicating that the $x = 0.05$ dopant amount is appropriate. This result could be explained by its best combination of Li^+ ion diffusion coefficient and electronic conductivity. It is also consistent with EIS results showing the smallest R_{ct} value for $\text{Li}_{3.9}\text{Ni}_{0.15}\text{Ti}_{4.95}\text{O}_{12}$ in Table 2. At 5 C , the capacity of $\text{Li}_{3.9}\text{Ni}_{0.15}\text{Ti}_{4.95}\text{O}_{12}$ is 118% higher than that of the pristine value, indicating that $\text{Li}_{3.9}\text{Ni}_{0.15}\text{Ti}_{4.95}\text{O}_{12}$ is superior compared to the heavily Ni^{2+} doped $\text{Li}_{11/3}\text{Ni}_{1/2}\text{Ti}_{29/6}\text{O}_{12}$ sample studied by Kim et al. [13] at this high rate.

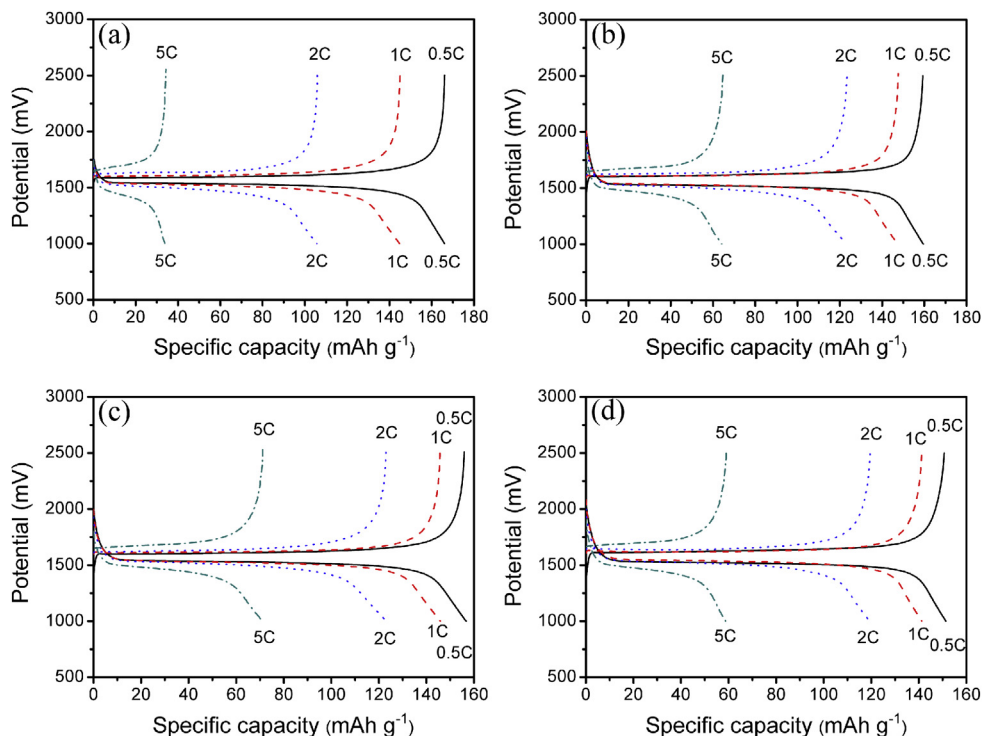


Fig. 8. Second discharge–charge curves of $\text{Li}_{4-2x}\text{Ni}_{3x}\text{Ti}_{5-x}\text{O}_{12}$ samples with (a) $x = 0$, (b) $x = 0.025$, (c) $x = 0.05$ and (d) $x = 0.075$ at 0.5 C , 1 C , 2 C and 5 C (identical discharge/charge rates were used).

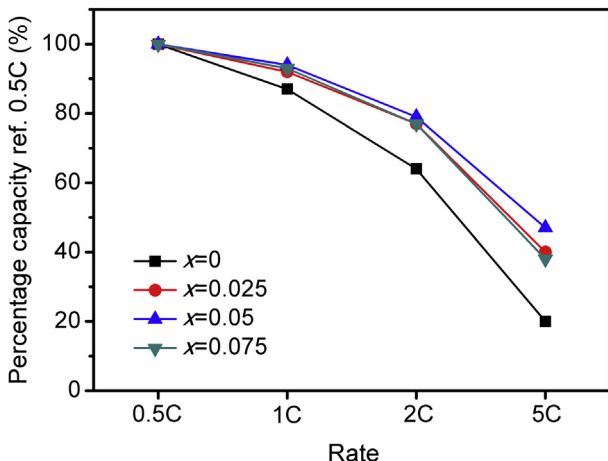


Fig. 10. Capacity retention of $\text{Li}_{4-2x}\text{Ni}_{3x}\text{Ti}_{5-x}\text{O}_{12}$ ($x = 0, 0.025, 0.05$ and 0.075) samples at 0.5 C , 1 C , 2 C and 5 C (identical discharge/charge rates were used).

4. Conclusions

In this research, $\text{Li}_{4-2x}\text{Ni}_{3x}\text{Ti}_{5-x}\text{O}_{12}$ ($0 \leq x \leq 0.25$) powders have been prepared through solid-state reaction method. All Ni^{2+} doped materials possess spinel structure with $\text{Fd}\bar{3}m$ space group without any impurities. They have similar lattice parameters and free blockages of Ni^{2+} in the 8a – 16c – 8a Li^+ transportation paths. Ni^{2+} doped samples have similar Li^+ ion diffusion coefficients to pristine one due to the negligible change in lattice parameter. The electrons in the 3d orbitals of Ni^{2+} ions contribute to the improved electronic conductivity. As a result, Ni^{2+} doped samples have good rate performance, of which $\text{Li}_{3.9}\text{Ni}_{0.15}\text{Ti}_{4.95}\text{O}_{12}$ is the best. At 5 C , it has a high capacity of 72 mAh g^{-1} which is 1.2 times larger than that of pristine one. Therefore, the novel Ni^{2+} doped $\text{Li}_4\text{Ti}_5\text{O}_{12}$ may find promising applications in EVs/HEVs due to its good rate performance and the simple synthesis route.

Acknowledgement

This research is supported by Agency for Science, Technology and Research, Singapore through the research grant R265-000-442-305 and A* Star Singapore-China Joint Research Programme (No. 2012DFG52130).

Appendix A. Supplementary data

Supplementary data related to this article can be found at <http://dx.doi.org/10.1016/j.jpowsour.2013.01.056>.

References

- M. Armand, J.M. Tarascon, *Nature* 451 (2008) 652–657.
- M. Yoshio, H.Y. Wang, K. Fukuda, Y. Hara, Y. Adachi, *J. Electrochem. Soc.* 147 (2000) 1245–1250.
- S.S. Zhang, K. Xu, T.R. Jow, *J. Power Sources* 160 (2006) 1349–1354.
- S.S. Zheng, *J. Power Sources* 161 (2006) 1385–1391.
- A.D. Robertson, L. Trevino, H. Tukamoto, J.T.S. Irvine, *J. Power Sources* 81–82 (1999) 352–357.
- K.M. Colbow, J.R. Dahn, R.R. Haering, *J. Power Sources* 26 (1989) 397–402.
- J.B. Goodenough, Y. Kim, *Chem. Mater.* 22 (2010) 587–603.
- T. Ohzuku, A. Ueda, N. Yamamoto, *J. Electrochem. Soc.* 142 (1995) 1431–1435.
- X. Li, M.Z. Qu, Z.L. Yu, *J. Alloy Compd.* 487 (2009) L12–L17.
- S.Z. Ji, J.Y. Zhang, W.W. Wang, Y. Huang, Z.R. Feng, Z.T. Zhang, Z.L. Tang, *Mater. Chem. Phys.* 123 (2010) 510–515.
- C.H. Chen, J.T. Vaughan, A.N. Jansen, D.W. Dees, A.J. Kahaian, T. Goacher, M.M. Thackeray, *J. Electrochem. Soc.* 148 (2001) A102–A104.
- B. Zhang, H.D. Du, B.H. Li, F.Y. Kang, *Electrochim. Solid-State Lett.* 13 (2010) A36–A38.
- J.S. Kim, S.W. Kim, H. Gwon, W.S. Yoon, K. Kang, *Electrochim. Acta* 54 (2009) 5914–5918.
- H.L. Zhao, Y. Li, Z.M. Zhu, J. Lin, Z.H. Tian, R.L. Wang, *Electrochim. Acta* 53 (2008) 7079–7083.
- T.F. Yi, Y. Xie, J. Shu, Z.H. Wang, C.B. Yue, R.S. Zhu, H.B. Qiao, *J. Electrochim. Soc.* 158 (2011) A266–A274.
- Z.J. Yu, X.F. Zhang, G.L. Yang, J. Liu, J.W. Wang, R.S. Wang, J.P. Zhang, *Electrochim. Acta* 56 (2011) 8611–8617.
- J. Wolfenstine, J.L. Allen, *J. Power Sources* 180 (2008) 582–585.
- Y.K. Sun, D.J. Jung, Y.S. Lee, K.S. Nahm, *J. Power Sources* 125 (2004) 242–245.
- Y.J. Hao, Q.Y. Lai, J.Z. Lu, X.Y. Ji, *Ionics* 13 (2007) 369–373.
- D. Yoshikawa, N. Suzuki, Y. Kadoma, K. Ui, N. Kumagai, *Funct. Mater. Lett.* 5 (2012) 125001.
- S.H. Huang, Z.Y. Wen, B. Lin, J.D. Han, X.G. Xu, *J. Alloy Compd.* 457 (2008) 400–403.
- S.H. Huang, Z.Y. Wen, J.C. Zhang, Z.H. Gu, X.H. Xu, *Solid State Ionics* 177 (2006) 851–855.
- M.W. Raja, S. Mahanty, M. Kundu, R.N. Basu, *J. Alloy Compd.* 468 (2009) 258–262.
- A.S. Prakash, P. Manikandan, K. Ramesha, M. Sathiya, J.M. Tarascon, A.K. Shukla, *Chem. Mater.* 22 (2010) 2857–2863.
- K. Naoi, S. Ishimoto, Y. Isobe, S. Aoyagi, *J. Power Sources* 195 (2010) 6250–6254.
- D. Bresser, E. Paillard, M. Copley, P. Bishop, M. Winter, S. Passerini, *J. Power Sources* 219 (2012) 217–222.
- K. Naoi, *Fuel Cells* 10 (2010) 825–833.
- J.Y. Kim, J. Cho, *Electrochim. Solid-State Lett.* 10 (2007) A81–A84.
- Y. Li, G.L. Pan, J.W. Liu, X.P. Gao, *J. Electrochim. Soc.* 156 (2009) 495–499.
- S.C. Lee, S.M. Lee, J.W. Lee, J.B. Lee, S.M. Lee, S.S. Han, H.C. Lee, H.J. Kim, *J. Phys. Chem. C* 113 (2009) 18420–18423.
- Z.S. Hong, T.B. Lan, F.Y. Xiao, H.X. Zhang, M.D. Wei, *Funct. Mater. Lett.* 4 (2011) 389–393.
- Y. Lv, H. Zhang, G.P. Cao, B.Y. Wang, X.D. Wang, *Mater. Res. Bull.* 46 (2011) 2312–2316.
- E. Kang, Y.S. Jung, G.H. Kim, J. Chun, U. Wiesner, A.C. Dillon, J.K. Kim, J. Lee, *Adv. Funct. Mater.* 21 (2011) 4349–4357.
- N.D. He, B.S. Wang, J.J. Huang, *J. Solid State Electrochem.* 14 (2010) 1241–1246.
- R.G. Burns, *Mineralogical Applications of Crystal Field Theory*, second ed., Cambridge University Press, Cambridge, 1993.
- A.C. Larson, R.B. Von Dreele, *General Structure Analysis System (GSAS)*, Los Alamos National Laboratory Report LAUR 86–748, 1994.
- B.H. Toby, *J. Appl. Cryst.* 34 (2001) 210–213.
- R.D. Shannon, *Acta Cryst.* A32 (1976) 751–767.
- H. Shiiba, M. Nakayama, M. Nogami, *Solid State Ionics* 181 (2010) 994–1001.
- S.H. Huang, Z.Y. Wen, X.J. Zhu, Z.X. Lin, *J. Power Sources* 165 (2007) 408–412.
- S.E. Dorris, T.O. Mason, *J. Am. Ceram. Soc.* 71 (1988) 379–385.
- D.C. Carter, T.O. Mason, *J. Am. Ceram. Soc.* 71 (1988) 213–218.
- M.A. Mousa, *Thermochim. Acta* 158 (1990) 177–181.
- D.T. Liu, C.Y. Ouyang, J. Shu, J. Jiang, Z.X. Wang, L.Q. Chen, *Phys. Stat. Sol. (b)* 243 (2006) 1835–1841.